

Performance improvement of a direct carbon solid oxide fuel cell through integrating an Otto heat engine

Haoran Xu^{1, 2, 4}, Bin Chen², Peng Tan², Houcheng Zhang^{1, 2,*}, Jinliang Yuan³, John T.S. Irvine⁴, Meng Ni^{2,*}

¹ Department of Microelectronic Science and Engineering, Ningbo University, Ningbo 315211, China

² Building Energy Research Group, Department of Building and Real Estate, The Hong Kong Polytechnic University, Hung Hom, Kowloon, Hong Kong, China

³ Faculty of Maritime and Transportation, Ningbo University, Ningbo 315211, China

⁴ School of Chemistry, University of St Andrews, St Andrews, Fife, KY16 9ST, UK

Abstract: A novel system consisting of an external heat source, a direct carbon solid oxide fuel cell (DC-SOFC), a regenerator and an air standard Otto cycle engine is proposed to improve the performance of the DC-SOFC. Considering the electrochemical/chemical reactions, ionic/electronic charge transport, mass/momentum transport and heat transfer, a 2D tubular DC-SOFC model shows that the overall heat released in the cell can be smaller than, equal to or larger than the heat required by the internal Boudouard reaction. Three different operating modes of the proposed system are identified, and accordingly, analytical expressions for the equivalent power output and efficiency of the proposed system are derived under different operating conditions. The modeling results show that the Otto heat engine can effectively recover the waste heat from the DC-SOFC for additional power production especially at large operating current density. Comprehensive parametric studies are conducted to investigate the effects of the different operating conditions of DC-SOFC on its performance and heat generation. The effects of compression ratio, internal irreversibility factor and power dissipation of the Otto heat engine on the system performance improvement are also studied.

Keywords: Solid oxide fuel cell; Carbon gasification; Air standard Otto heat engine;

28 Performance improvement; Parametric study

29

30 *Corresponding authors.

31 Email addresses: zhanghoucheng@nbu.edu.cn (H. Zhang), bsmengni@polyu.edu.hk (M. Ni).

1. Introduction

The increasing global attention on energy crisis drives worldwide research interest in clean and high efficiency energy conversion devices, such as solid oxide fuel cells (SOFCs). SOFCs are all solid-state devices working at a high temperature (e.g. 800°C). A typical SOFC has a sandwiched structure with a dense electrolyte between a porous anode and a porous cathode [1-3]. Fuels (e.g. H₂) and oxidants (e.g. O₂) are supplied to the anode and cathode, respectively. Through electrochemical reactions, chemical energy in fuels and oxidants can be converted into electrical power directly with a high efficiency. As fuels and oxidants are separated by the dense electrolyte, the post-process of emission gases is relatively easy.

Apart from gas fuels like H₂ and CO, the utilization of solid carbons in SOFCs has received rising attention as these widely spreaded solid fuels have high volumetric energy density, which can easily be obtained at a low cost. There are two main methods for direct solid carbon utilization in the SOFCs. One is electrochemical oxidation of solid carbon that is in direct contact with the electrode catalyst (usually called as direct carbon fuel cell, DCFC) [1, 2], aiming for a high thermodynamic efficiency. However, this method yields a low power density due to difficult transport of solid carbon and poor contact between the carbon particles and the electrochemical reaction sites (triple phase boundaries: TPBs). The other method is solid carbon indirect utilization through an agent (usually called as direct-carbon solid oxide fuel cell, DC-SOFC), which converts solid carbon into gas fuel such as CO for the electrochemical reaction at the TPBs [3, 4]. Compared with the first method, the second method provides a much higher power density due to easy gas transport and good contact between gas fuel and the TPBs. With verifications of its mechanism [5, 6], catalysts are developed to further improve the performance of DC-SOFCs [7-10]. Besides, the concept of CO and electrical power co-generation is proposed and analyzed. The results suggest that a much higher exergy efficiency can be achieved by the DC-SOFC than DCFC [11]. Different agents have also been compared to explore the application of DC-SOFC[12]. It is found that DC-SOFC with H₂O as

gasification agent for H_2 and CO production could achieve higher performance than that with CO_2 agent due to fast gasification kinetics using H_2O agent and low activation loss associated with H_2 electrochemical oxidation. To further understand the detailed chemical/physical process in the DC-SOFCs, mathematical models are developed [13-16]. Our recent mathematical model analyses [17] prove the existence of heat balance in DC-SOFC when it operates at a relative low current density. When the DC-SOFC operates at a high current density to provide a large power density, the heat generated from the irreversible electrochemical losses and enthalpy change exceeds the heat demand by Boudouard reaction. Therefore, the efficiency of DC-SOFCs can be further improved at a wide range of operating current density by utilizing the waste heat [18].

Various thermodynamic cycles including Carnot cycle[19], Stirling cycle[20], Ericsson cycle[21], Brayton cycle[22], Rankine cycle[23], Braysson cycle[24] and Kalina cycle[25] have been used for the conversion of heat into power. Compared with these cycles, Otto cycle has interesting perspectives as the rapid combustion process takes place at a constant volume, which indicates an excellent potential to integrate with other systems. By applying the air-standard analysis on Otto cycle, a number of modeling works have been conducted on air-standard Otto cycle heat engines [26-29] to illustrate the thermodynamic aspects of engine performance. Gumus et al.[30] compared the performance of a reversible Otto cycle based on its maximum power, maximum power density and maximum efficient power, where they conclude that the design parameters at maximum efficient power conditions lead to more efficient engines than that at the maximum power condition. Besides, the maximum efficient power criterion may have a significant power advantage compared with maximum power density criterion. By considering multiple irreversible losses, Zhao et al. [31, 32] evaluated the performance of an irreversible Otto heat engine and determined the optimum criteria. Chen et al. [33] further evaluated the performance of the air-standard Otto cycle with different specific heats of working fluid [34, 35] by using different objective functions and heat transfer laws. Apart from aforementioned works focusing on Otto heat engine itself, there is another work done by Eldighidy [36], where an air-standard Otto cycle is proposed to harvest solar energy

for power generation. Obviously, it is a feasible method for the air-standard Otto cycle heat engine to harvest the waste heat from DC-SOFC for performance improvement. An up-to-date literature survey shows that there is no work reported on this subject.

In this work, a numerical model is developed to analyze the performance improvement of DC-SOFC by combining it with an air-standard Otto cycle heat engine. Based on the numerical analysis, three system operation modes are specified under different operating conditions. Besides, the performance of the proposed system is evaluated based on the output power and efficiency expressions. The advantages of the system are also demonstrated through numerical calculations. Finally, the effects of several design parameters and operating conditions on the performance of the system are discussed.

2. System description

As shown in Fig. 1 (a), the proposed system mainly consists of a DC-SOFC, an external heat source, an air standard Otto cycle heat engine and a regenerator. The DC-SOFC generates electrical power P_{SOFC} (W) by consuming solid carbon. To ensure the normal operation of the DC-SOFC, certain amount of heat Q (J S^{-1}) should be provided to DC-SOFC at low operating current density (DC-SOFC in the endothermic mode), and the corresponding heat and mass transfer are shown in Fig. 1 (b). Otherwise, the air standard Otto cycle heat engine should be connected to utilize the waste heat from the DC-SOFC for additional power (P_{Otto}) production, and the corresponding heat and mass transfer are shown in Fig. 1 (c). It should be noted that the CO reformation process is inside the anode of the DC-SOFC, and the excess heat generated in the SOFC component is carried out by the outlet products to power the Otto engine for additional power generation. In calculation, partial differential equations for CO reformation and SOFC component are coupled in COMSOL MULTIPHYSICS®. The generated heat (an output variable from DC-SOFC) is then an input variable in the calculation of Otto engine. The regenerator in the system preheats the inlet solid carbon and gas by outlet high-temperature gases.

For simplification, the following assumptions are adopted [15]

- Electrochemical reactions spatially take place at triple phase boundaries (TPBs), which are assumed to be uniformly distributed in the porous electrodes. Electronic and ionic conduction phases in the porous electrodes are continuous and homogeneous;
- Ionic and electronic charge transport processes take place in the PEN (Positive Electrode-Electrolyte-Negative electrode assembly), and the charge transfer reaction can take place at TPB sites throughout the porous electrode;
- All gases (CO , CO_2 , O_2 and N_2) involved in the DC-SOFC are ideal gases and the gas flow is incompressible;
- Internal relaxation times in the adiabatic processes are negligible;
- Heat transfer irreversibility between the DC-SOFC and the Otto heat engine is neglected;
- Irreversibility in the two adiabatic processes is neglected;
- Working substance air of Otto heat engine is assumed to behave as an ideal gas.

2.1 DC-SOFC

In DC-SOFCs, solid carbon in anode chamber is gasified by CO_2 to generate CO molecules, which then diffuse into the porous anode and react with O^{2-} ions at the TPB sites. The produced CO_2 molecules in electrochemical reactions subsequently diffuse back to the anode chamber and continue the Boudouard reaction for CO generation. These processes repeat between the anode chamber and the porous anode for power generation as long as there is enough solid carbon in the anode chamber.

A previously developed 2D numerical model is adopted to describe the electrochemical /chemical reactions, ionic/electronic charge transport, mass/momentum transport and heat transfer in the tubular DC-SOFC.

2.1.1 Chemical reaction model

In anode chamber, the Boudouard reaction converts solid carbon into CO by consuming

140 CO₂, i.e.,
 141 $C + CO_2 = 2CO$. (1)

142 Its reaction rate can be calculated as [37]

$$143 R_{rb} = k_{rb} \exp(-E_{rb}/RT) c_{CO_2}. \quad (2)$$

144 2.1.2 Electrochemical reaction model

145 At anode TPB sites, CO molecules electrochemically react with O²⁻ ions and release
 146 electrons, i.e.,



148 The above mentioned O²⁻ ions are transported from cathode TPB sites, where O₂ molecules
 149 are reduced into O²⁻, i.e.,



151 The equilibrium potential (E_{CO}) for above reactions can be determined by [38]

$$152 E_{CO} = E_{CO}^0 + \frac{RT}{2F} \ln \left[\frac{P_{CO}^L (P_{O_2}^L)^{1/2}}{P_{CO_2}^L} \right], \quad (5)$$

153 where R is the universal gas constant and F is Faraday constant. T is operating temperature and

154 P^L is local gas partial pressure. E_{CO}^0 is the standard potential (V), which can be calculated by

$$155 E_{CO}^0 = 1.46713 - 0.0004527T. \quad (6)$$

156 For the calculation of the operating potential (E), both activation overpotential (η_{act}) and
 157 ohmic overpotential (η_{ohmic}) should be considered, i.e.,

$$158 E = E_{CO}^0 - \eta_{act} - \eta_{ohmic} \quad (7)$$

159 The relationship between current density and above two overpotential losses are described
 160 by Butler-Volmer equation (Eq. (8)) and ohm law (Eq. (9)), respectively[39], i.e.,

$$161 i = i_0 \left\{ \exp \left(\frac{\alpha n F \eta_{act}}{RT} \right) - \exp \left(- \frac{(1-\alpha) n F \eta_{act}}{RT} \right) \right\}, \quad (8)$$

162 and

$$i = -\sigma^{\text{eff}} \nabla(\phi), \quad (9)$$

where i is operating current density, i_0 is exchange current density, α is the electron transfer coefficient and n is the number of transferred electrons per electrochemical reaction. σ^{eff} and ϕ are effective conductivity (S m^{-1}) and electric potential (V), respectively.

2.1.3 Mass and momentum transport model

Mass and momentum transport are, respectively, calculated by the extended Fick's model (Eq. (10)) and Navier-Stokes equation (Eq. (11)) [15], i.e.,

$$N_m = -\frac{1}{RT} \left(\frac{B_0 y_m P}{\mu} \frac{\partial P}{\partial z} - D_m^{\text{eff}} \frac{\partial (y_m P)}{\partial z} \right) \quad (m = 1, 2, \dots, l), \quad (10)$$

and

$$\rho \frac{\partial u}{\partial t} + \rho u \nabla u = -\nabla p + \nabla [\mu (\nabla u + (\nabla u)^T) - \frac{2}{3} \mu \nabla u] - \frac{\varepsilon \mu u}{k}, \quad (11)$$

where B_0 is the permeability (m^2) of the porous electrodes, y_m is the mole fraction of component m , μ is the gas viscosity ($\text{N m}^{-1} \text{s}^{-1}$), D_m^{eff} is the overall effective diffusion coefficient ($\text{m}^2 \text{s}^{-1}$) of component m , ρ (kg m^{-3}) is the gas density and u (m s^{-1}) is the velocity vector.

2.1.4 Heat transfer model

The heat transfer process is described by the general heat balance equation [17]

$$\rho C_p u \cdot \nabla T + \nabla \cdot (-\lambda_{\text{eff}} \nabla T) = Q, \quad (12)$$

where C_p is the heat capacity, u is the fluid velocity field, λ_{eff} is the effective heat conductivity and Q is the heat source term.

The above model is validated by fitting simulation results (I - V characteristics) with

experimental data and good agreement has been found in Ref. [17]. The DC-SOFC model is described by partial differential equations, which are handled by nonlinear finite elements method using commercial software COMSOL MULTIPHYSICS®.

The power output of the DC-SOFC is determined by

$$P_{\text{SOFC}} = V \times I, \quad (13)$$

where V (V) and I (A) are output voltage and current, respectively.

Considering the irreversible polarization losses and enthalpy changes in DC-SOFC, its electrical efficiency

$$\eta_{\text{SOFC}} = \frac{P_{\text{SOFC}}}{P_{\text{SOFC}} + Q} \quad (14)$$

can be defined, where Q (J s^{-1}) is the overall heat released from the DC-SOFC, which is defined as positive in this paper. The heat Q can be further expressed as

$$Q = Q_e - Q_c, \quad (15)$$

where Q_c (J s^{-1}) is the absorbed heat by the Boudouard reaction and Q_e (J s^{-1}) includes heat released from the electrochemical reaction and overpotential losses. Thus, Q_e can be calculated as

$$Q_e = -T\Delta S \times \frac{I}{2F} + (E - V)I. \quad (16)$$

When $Q_e = Q_c$, i.e., $Q = 0$, the thermal neutral current

$$I_{\text{tn}} = \frac{Q_c}{-T\Delta S/2F + E - V_{\text{tn}}} \quad (17)$$

can be obtained, where V_{tn} (V) is the thermal neutral voltage corresponding to I_{tn} .

Based on the above governing equations and parameters in Table 1, the relationship between Q and operating current density i ($i = I/A$, A m^{-2}) are obtained as shown in Fig. 2. It is seen that Q increases from negative to positive values with increasing current density. When $i < i_{\text{tn}}$, i.e., $Q < 0$, the heat produced due to the polarization losses and enthalpy change of the electrochemical reaction is less than the heat required for the Boudouard reaction. Certain amount of heat $|Q|$ should be supplied from the external heat source to the DC-SOFC to maintain its operating temperature. In this case, the external heat source in Fig. 1(a) should be switched on while the air standard Otto heat engine is off. When $i = i_{\text{tn}}$, i.e., $Q = 0$, the

heat generation equals the heat consumption by Boudouard reaction in the DC-SOFC, which means the DC-SOFC can work in a thermally self-sustained manner. When $i > i_{tn}$, i.e., $Q > 0$, the heat generated exceeds the required heat for the Boudouard reaction. The air standard Otto heat engine should be switched on to utilize the waste heat from DC-SOFC for extra electrical power (P_{Otto}) generation. As also shown in Fig. 2, a larger i_{tn} is needed at a higher operating temperature to generate more heat for the endothermic Boudouard reaction. Less netheat is generated for a given current density at a higher operating temperature, as the faster Boudouard reaction at a higher temperature consumes more heat from DC-SOFC.

2.2 Air standard Otto cycle heat engine

The air standard Otto cycle is composed of two adiabatic processes (1→2 and 3→4) and two isochoric processes (2→3 and 4→1), as shown in Fig. 3. T_1 , T_2 , T_3 and T_4 are temperatures of the working substance at the state points 1, 2, 3 and 4. The heat flow from the DC-SOFC, Q , is provided to the Otto cycle heat engine at the volume V_2 . After producing power P_{Otto} , the remaining heat Q_r is released at the volume V_2 . Considering instantaneous adiabats, the period of the Otto cycle [40]

$$\tau_t = t_{1V} + t_{2V} = K_1(T_3 - T_2) + K_2(T_4 - T_1) \quad (18)$$

can be calculated, where t_{1V} and t_{2V} are, respectively, the heating and cooling times; K_1 and K_2 are temperature-independent constants ($s K^{-1}$).

From the first law of thermodynamics, the reversible work

$$W_{Otto,r} = C_{V_1}(T_3 - T_2) - C_{V_2}(T_4 - T_1) \quad (19)$$

done by the Otto cycle heat engine can be calculated, where C_{V_1} and C_{V_2} are the heat capacities of gases in the compression and power strokes, respectively.

Thus, the reversible power is shown as

$$P_{Otto,r} = \frac{W_{Otto,r}}{\tau_t} = \frac{C_{V_1}(T_3 - T_2) - C_{V_2}(T_4 - T_1)}{K_1(T_3 - T_2) + K_2(T_4 - T_1)}. \quad (20)$$

If the reversible work with adiabats given by $TV^{(\gamma-1)} = \text{constant}$, then Eq. (20) can be further rewritten as [40, 41]

$$P_{\text{Otto},r} = \frac{C_{V_1} - C_{V_2} r^{(1-\gamma)}}{K_1 + K_2 r^{(1-\gamma)}}, \quad (21)$$

where $\gamma = C_p / C_v$, C_p and C_v are, respectively, constant-pressure heat capacity (J K^{-1}) and constant-volume heat capacity (J K^{-1}), and $r = V_1/V_2$ is the compression ratio.

Considering a dissipation term represented by a friction force proportional to the velocity, the friction force

$$F_f = -\omega v = -\omega \frac{dx}{dt} \quad (22)$$

can be obtained, where ω is the friction coefficient which takes into account the global losses, v is the piston velocity, and x is the piston displacement. Then, the friction-related power loss

$$P_f = -\omega \frac{dx}{dt} \frac{dx}{dt} = -\omega v^2 \quad (23)$$

can be calculated [41].

The piston mean velocity can be expressed as

$$\bar{v} = \frac{x_1 - x_2}{\Delta t_{12}} = \frac{x_2(r-1)}{\Delta t_{12}}, \quad (24)$$

where x_2 is the piston position at minimum volume and Δt_{12} is the time spent in the power stroke. Counted the piston friction-like losses, the power output is reduced from $P_{\text{Otto},r}$ to

$$P_{\text{Otto},P} = P_{\text{Otto},r} - P_f = \frac{C_{V_1} - C_{V_2} r^{(1-\gamma)}}{K_1 + K_2 r^{(1-\gamma)}} - b(r-1)^2, \quad (25)$$

$$\text{where } b = \frac{\omega x_2^2}{(\Delta t_{12})^2}.$$

In addition to the piston friction-like losses, irreversible losses from mass transfer, friction, eddy and other irreversible effects inside the cyclic working fluid should be considered. The total irreversible effects within the working fluid can be characterized by the internal

258 irreversibility factor [40]

$$259 \quad I_R = \frac{\Delta S_{W1}}{|\Delta S_{W2}|} = \frac{C_{V1} \ln(T_3/T_2)}{C_{V2} \ln(T_4/T_1)} = \frac{C_{V1}}{C_{V2}}, \quad (26)$$

260 where ΔS_{W1} and ΔS_{W2} are entropy changes ($J K^{-1}$) along the hot isothermal branch and the
 261 cold isothermal compression branch. The internal irreversibility factor is in the range of
 262 $0 < I_R \leq 1$.

263 Considering the finite-time evolution of the cycle's compression and power strokes, piston
 264 friction-like losses and internal irreversibility of working fluid, the efficiency and power output
 265 of the air standard Otto heat engine are, respectively, given by [40-42]

$$266 \quad \eta_{Otto} = 1 - r^{1-\gamma} - \frac{b(r-1)^2}{C_{V2}} (K_1 + K_2 r^{1-\gamma}), \quad (27)$$

267 and

$$268 \quad P_{Otto} = Q \left[1 - r^{1-\gamma} - \frac{b(r-1)^2}{C_{V2}} (K_1 + K_2 r^{1-\gamma}) \right], \quad (28)$$

269 where the relevant parameters for the air standard Otto cycle are summarized in Table 2.

270

271 **2.3 The regenerator**

272 The regenerator works as a heat exchanger continuously preheating the inlet solid carbon
 273 and air by the high-temperature outlet gases. The products are cooled down to the
 274 environmental temperature with the solid carbon and oxygen being heated to the operating
 275 temperature of the DC-SOFC. According to the thermodynamic parameters given in Ref. [18],
 276 one can prove that

$$277 \quad \Delta Q_{CO} - (\Delta Q_C + \Delta Q_{1O_2}) > 0, \quad (29)$$

278 and

$$279 \quad \Delta Q_{CO_2} - (\Delta Q_C + \Delta Q_{2O_2}) > 0, \quad (30)$$

280 where $\Delta Q_{CO} = \dot{m} \int_{T_0}^T C_{CO} d\tau$, $\Delta Q_C = \dot{m} \int_{T_0}^T C_C d\tau$, $\Delta Q_{1O_2} = 0.5 \dot{m} \int_{T_0}^T C_{O_2} d\tau$, $\Delta Q_{2O_2} = \dot{m} \int_{T_0}^T C_{O_2} d\tau$,

$\Delta Q_{\text{CO}_2} = \dot{m} \int_{T_0}^T C_{\text{CO}_2} d\tau$, \dot{m} is the molar consumption rate of solid carbon, T_0 is the ambient temperature (K), C_j is the isobaric molar heat capacities ($\text{J mol}^{-1} \text{K}^{-1}$) for species j (j = solid carbon, CO, O₂ or CO₂). As only CO and CO₂ are present in the anode outlet gas, we can conclude that the heat contained in the products is always enough to preheat the reactants to attain the operating temperature of the DC-SOFC regardless of its molar fraction of CO and CO₂ (the inlet N₂ in air is supposed to be preheated by the outlet N₂). Since some high-effectiveness regenerators have already been reported [43], it is appropriate to assume that the regenerator in Fig. 1 (a) performs perfect regeneration.

2.4 The performance of the proposed system

As the waste heat from DC-SOFC is used to preheat the activated carbon and air at the inlet of the cell, the heat loss from the DC-SOFC system to the environment is negligible against the electrical power (P_{SOFC}). Adding the contribution of the air standard Otto cycle heat engine, the equivalent power output (P) and equivalent efficiency (η) of the proposed system can be, respectively, expressed as

$$P = \begin{cases} = P_{\text{SOFC}} & (i < i_{\text{tn}}) \\ = P_{\text{SOFC}} + P_{\text{Otto}} & (i \geq i_{\text{tn}}) \end{cases}, \quad (31)$$

and

$$\eta = \begin{cases} = \frac{P_{\text{SOFC}}}{P_{\text{SOFC}} + |Q|} & (i < i_{\text{tn}}) \\ = \frac{P_{\text{SOFC}} + P_{\text{Otto}}}{P_{\text{SOFC}} + Q} & (i \geq i_{\text{tn}}) \end{cases}. \quad (32)$$

3. Results and discussion

Based on the mathematical models above which have been well validated by the previous studies[15] and relevant parameters given in Table 1 and Table 2, the performance characteristics of the proposed system can be analyzed. The parameters are taken as default

ones unless they are specifically mentioned.

3.1 Performance characteristics of air standard Otto heat engine

The basic performance characteristics of the air standard Otto heat engine are shown in Fig. 4. As can be found in Fig. 4 (a), the efficiency (η_{Otto}) increases with increasing compression ratio (r) at different power dissipation (b) values at the beginning. After reaching the peak efficiency values, η_{Otto} decreases with a further increase in compression value. Besides, a higher efficiency and larger effective interval compression ratio can be achieved at smaller power dissipation value. When power dissipation is decreased to zero, the friction losses in the Otto heat engine can be negligible. In this situation, Eqs. (27) and (28) can be, respectively, reduced into

$$\eta_{\text{Otto}} = 1 - r^{1-\gamma} / I_R, \quad (33)$$

and

$$P_{\text{Otto}} = Q \left(1 - r^{1-\gamma} / I_R \right). \quad (34)$$

As can be found in Fig. 4(b), the equivalent power density of the air standard Otto heat engine P_{Otto}^* increases with the increasing operating current density of the DC-SOFC i and the increasing internal irreversibility factor I_R . The effect of the internal irreversibility factor on its power output becomes more significant at larger operating current density as more heat is generated from DC-SOFC. With the internal irreversibility factor reaching 1, the Otto heat engine achieves its upper limit power density. In this situation, Eqs. (27) and (28) can be, respectively, reduced into

$$\eta_{\text{Otto}} = 1 - r^{1-\gamma} - \frac{b(r-1)^2}{C_{V_2}} (K_1 + K_2 r^{1-\gamma}), \quad (35)$$

and

$$P_{\text{Otto}} = Q \left[1 - r^{1-\gamma} - \frac{b(r-1)^2}{C_{V_2}} (K_1 + K_2 r^{1-\gamma}) \right]. \quad (36)$$

3.2 Power density improvement of the proposed system

The equivalent power densities of the DC-SOFC, Otto heat engine and proposed system are compared at different operating temperatures as shown in Fig. 5, where $P_{\text{SOFC}}^* = P_{\text{SOFC}}/A$ and $P^* = P/A$ are the power densities for the DC-SOFC and the proposed system, respectively. When $i \leq i_{\text{tn}}$, the curves of $P^* \sim i$ and $P_{\text{SOFC}}^* \sim i$ are overlapped as no waste heat is transferred to Otto heat engine for extra power production. In the range of $i > i_{\text{tn}}$, P_{Otto}^* keeps growing with larger operating current density as more heat is provided from the DC-SOFC. While for the DC-SOFC, its power density P_{SOFC}^* first increases and then decreases with the increasing i . As a result, the power density is significantly improved in the proposed system and P^* increases to attain a maximum value with increasing i .

The elevated operating temperature improves the performance of the DC-SOFC by promoting its chemical/electrochemical reactivity and ionic conductivity. However, the power density of the Otto heat engine at the same operating current density decreases with increasing operating temperature due to less waste heat supply, as shown by Fig. 2. As P_{SOFC}^* is more sensitive to the operating temperature than P_{Otto}^* , a higher operating temperature is preferred for the proposed system to obtain a higher output power density. For example, when the DC-SOFC works at a current density of 30000 A m^{-2} , the equivalent power density of the proposed system approximately increases from 5550 W m^{-2} at 1073 K to 7950 W m^{-2} at 1173 K , which are about 79.6% and 33.3% larger than that of the stand-alone DC-SOFC, respectively.

3.3 Efficiency characteristics of proposed system

Apart from power density, the equivalent efficiencies of the DC-SOFC, Otto heat engine and proposed system under different operating temperature are also compared as shown in Fig. 6. Similarly, the $\eta \sim i$ and $\eta_{\text{SOFC}} \sim i$ curves are overlapped in the region of $i \leq i_{\text{tn}}$ and the proposed system has the largest efficiency η when $i > i_{\text{tn}}$. The efficiency of the DC-SOFC is

quite high at small operating current density, where it reaches a peak efficiency of 100% at i_{in} as DC-SOFC is thermally self-sustained. With a further increase in operating current density, η_{SOFC} decreases to less than η_{Otto} (which does not vary with the operating temperature). When the DC-SOFC works at a current density of 30000 A m⁻², the equivalent efficiency of the proposed system increases from 46.8% at 1073 K to 60.8% at 1173 K mainly due to the significant efficiency improvement of the DC-SOFC, whose efficiency increases from 26.4% at 1073 K to 45.4% at 1173 K. A higher operating temperature is thus more favored to obtain a higher efficiency of the proposed system.

3.4 Effect of distance between carbon layer and anode electrode

In DC-SOFCs, the distance between carbon layer and anode (D_{ce}) will increase over time due to the consumption of solid carbon, resulting in the change of z in Eq. (10). As a result, the gas transportation between carbon layer and anode significantly affects the power output and heat generation in the proposed system. As shown in Fig. 7, as the distance between carbon layer and anode is decreased from 559 μ m to 59 μ m, a significant output power density improvement of the proposed system is found. The peak power density of the proposed system increases from 5030 W m⁻² at 559 μ m to 6990 W m⁻² at 59 μ m. As analyzed in our previous papers [15, 17], a small distance between carbon layer and anode helps to maintain a high fuel concentration in anode, which brings in a high output power density. Meanwhile, more heat can be provided from the DC-SOFC at higher operating current density, allowing more power to be generated through Otto heat engine. As a result, higher power density and efficiency of the proposed system can be obtained at a smaller distance, and this effect becomes more pronounced at a larger current density.

3.5 Effect of compression ratio

The effect of compression ratio (r) on the performance of the proposed system appears only in the region of $i > i_{in}$, as shown in Fig. 8. For a given current density, it is observed that

there exists peak values for the power density and efficiency of the proposed system with the change of compression ratio, indicating the existence of an optimum compression ratio. Based on the parameters given in Table 1 and Table 2, the optimum value for the compression ratio is found to be 9.26. Moreover, the optimum value for the compression ratio is closely related to the friction-like coefficient. The optimum value of compression ratio (r_{opt}) under different dissipation power (b) are listed in Table 3 by using the extremum condition $\partial\eta_{Otto}/\partial r = 0$, from which a smaller r_{opt} can be found at a larger b . It can be also found from Fig. 8 that the effect of compression ratio on the performance of the proposed system becomes more significant as the operating current density increases.

3.6 Effect of internal irreversibility factor and dissipation power

The effects of internal irreversibility factor (I_R) and dissipation power (b) on the performance of the proposed system are shown in Fig. 9, where the involved values of compression ratio are assigned from Table 3 to maximize the efficiency of the Otto heat engine. In the region of $i > i_{tn}$, significant effects of irreversibility factor and dissipation power can be found at large operating current density as more heat is provided from the DC-SOFC to the Otto heat engine. The power density and efficiency of the proposed system both increase with increasing I_R or decreasing b . When both the internal irreversible losses and the friction-like losses are negligible, the power density and efficiency of the proposed system can be drawn as the black square lines in Fig. 9. In this situation, Eqs. (27) and (28) can be reduced into

$$\eta_{Otto} = 1 - r^{1-\gamma}, \quad (37)$$

and

$$P_{Otto} = Q(1 - r^{1-\gamma}). \quad (38)$$

4. Conclusions

The previously developed 2D tubular DC-SOFC model shows that the overall heat generated in the cell could be smaller than, equal to or higher than the heat demand by the internal Boudouard reaction. A novel hybrid system consists of a DC-SOFC, an external heat source, a regenerator and an Otto heat engine is proposed to improve the performance of the DC-SOFC. Based on the thermal characteristics of the DC-SOFC, three operation modes are presented. The analytical expressions for the proposed system under different operating conditions are derived to evaluate its performance. The results show that the proposed system is technically feasible and effective, and the equivalent power density of the proposed system could be increased by up to 80% compared to the stand-alone DC-SOFC. Comprehensive parametric studies show that there exists an optimum value for the compression ratio to maximize the efficiency of the Otto heat engine, and increasing the operating temperature, operating current density and internal irreversibility factor will increase the overall power density and efficiency of the proposed system. Furthermore, decreasing dissipation power and the distance between carbon layer and anode electrode are also benefit to improve the equivalent power density and efficiency of the DC-SOFC based hybrid system.

Acknowledgement

This research is supported by the Natural Science Foundation of Zhejiang Province (Grant No. LQ14E060001), National Natural Science Foundation of China (Grant No. 51406091), a grant (PolyU 152127/14E) from Research Grant Council, University Grants Committee, Hong Kong SAR, a grant from Environment and Conservation Fund (ECF 54/2015), Hong Kong SAR, and the K. C. Wong Magna Fund in Ningbo University.

427 Nomenclature

428 Abbreviation

CHP	Combined heat and power
DC-SOFC	Direct-carbon solid oxide fuel cell
LSM	Strontium-doped lanthanum manganite
Otto	Otto heat engine
SCCM	Standard cubic centime per minute
SOFC	Solid oxide fuel cell
TPB	Triple phase boundary
YSZ	Yttrium stabilized zirconium

429

430 Roman

b	Power dissipation due to friction, W
B_0	Permeability coefficient, m^2
c_{CO_2}	Molar concentration of carbon dioxide, $\text{mol}\cdot\text{m}^{-3}$
C_p	C_p is constant-pressure heat capacity, $\text{J}\cdot\text{K}^{-1}$
C_v	C_v is constant-volume heat capacity, $\text{J}\cdot\text{K}^{-1}$
C_{V_1}	Heat capacity of the gases in the compression stroke, $\text{J}\cdot\text{K}^{-1}$
C_{V_2}	Heat capacity of the gases in the power strokes, $\text{J}\cdot\text{K}^{-1}$
D_{ce}	Distance between carbon layer and anode, μm
D_m^{eff}	Effective diffusivity of species m , $\text{m}^2\cdot\text{s}^{-1}$
E_{act}	Activation energy, $\text{J}\cdot\text{mol}^{-1}$
E_{CO}	Equilibrium potential for carbon monoxide oxidization, V
E_{CO}^0	Standard equilibrium potential for carbon monoxide oxidization, V

E_{eq}	Equilibrium Nernst potential, V
F	Faraday constant, $96485 \text{ C} \cdot \text{mol}^{-1}$
F_f	Friction force, N
i_o	Exchange current density, $\text{A} \cdot \text{m}^{-2}$
I	Electrical current, A
I_R	Internal irreversibility factor
$K_1 ; K_2$	Constant temperature rate in Eq. (18), (s K^{-1})
n	Number of electrons transferred per electrochemical reaction
N_i	Flux of mass transport, $\text{kg} \cdot \text{m}^{-3} \cdot \text{s}^{-1}$
p	(partial) Pressure, Pa
P	Power output, W
P_f	Friction-related power loss, W
$P_{Otto,r}$	Reversible power of the Otto heat engine, W
r	Compression ratio
R	Gas constant, $8.314 \text{ J} \cdot \text{mol}^{-1} \cdot \text{K}^{-1}$
R_{ce}	Reaction rate of Boudouard reaction, $\text{mol} \cdot \text{m}^{-3} \cdot \text{s}^{-1}$
ΔS_{W1}	Entropy change along the hot isothermal branch, $\text{J} \cdot \text{K}^{-1}$
ΔS_{W2}	Entropy change along the cold isothermal compression branch, $\text{J} \cdot \text{K}^{-1}$
Δt_{12}	Time spent in the power stroke, s
T	Temperature, K
$T_{1\sim 4}$	Temperatures of the working substance at the state points 1, 2, 3 and 4
u	Velocity field, $\text{m}^3 \cdot \text{s}^{-1}$
V	Volume fraction
V_1	Working substance volume along the constant-volume cooling branch, m^3

V_2 Working substance volumes along the constant-volume heating branch, m^3

$W_{\text{Otto},r}$ Reversible work of the Otto heat engine, W

x_2 Piston position at minimum volume, m

y_k Molar fraction of component k

Greek letters

α Charge transfer coefficient

β_{H_2} Electrochemical kinetics parameter for H_2

γ Ratio of specific heats

ε Porosity

η Efficiency

η_{act} Activation polarization, V

η_{ohmic} Ohmic polarization, V

κ Permeability, m^2

λ Thermal conductivity, $\text{W} \cdot \text{m}^{-1} \text{K}^{-1}$

μ Dynamic viscosity of fluid, $\text{Pa} \cdot \text{s}$

θ Friction coefficient, $\text{J} \cdot \text{s} \cdot \text{m}^{-2}$

ρ Fluid density, $\text{kg} \cdot \text{m}^{-3}$

σ Conductivity, S/m

τ Tortuosity

τ_t Period of the Otto cycle, s

\emptyset Potential, V

Subscripts

an Anode

ca Cathode

CO Carbon monoxide

CO₂ Carbon dioxide

H₂ Hydrogen

l Ionic phase

O₂ Oxygen

r Reversible

s Electronic phase

Superscripts

0 Parameter at equilibrium conditions

eff Effective

L Local

431

432 **References**

- 433 [1] Nurnberger S, Bu, Desclaux P, Franke B, Rzepka M, Stimming U. Direct carbon
434 conversion in a SOFC-system with a non-porous anode. *Energy & Environmental Science*.
435 2010;3:150-3.
- 436 [2] Li C, Shi Y, Cai N. Mechanism for carbon direct electrochemical reactions in a solid
437 oxide electrolyte direct carbon fuel cell. *Journal of Power Sources*. 2011;196:754-63.
- 438 [3] Bai Y, Liu Y, Tang Y, Xie Y, Liu J. Direct carbon solid oxide Fuel Cell—a potential high
439 performance battery. *International Journal of Hydrogen Energy*. 2011;36:9189-94.
- 440 [4] Yang B, Ran R, Zhong Y, Su C, Tadé MO, Shao Z. A carbon-air battery for high power
441 generation. *Angewandte Chemie - International Edition*. 2015;54:3722-5.
- 442 [5] Xie Y, Tang Y, Liu J. A verification of the reaction mechanism of direct carbon solid
443 oxide fuel cells. *Journal of Solid State Electrochemistry*. 2012;17:121-7.
- 444 [6] Cai W, Liu J, Xie Y, Xiao J, Liu M. An investigation on the kinetics of direct carbon solid
445 oxide fuel cells. *Journal of Solid State Electrochemistry*. 2016;20:2207-16.
- 446 [7] Wu Y, Su C, Zhang C, Ran R, Shao Z. A new carbon fuel cell with high power output
447 by integrating with in situ catalytic reverse Boudouard reaction. *Electrochemistry*
448 *Communications*. 2009;11:1265-8.
- 449 [8] Li C, Shi Y, Cai N. Performance improvement of direct carbon fuel cell by introducing
450 catalytic gasification process. *Journal of Power Sources*. 2010;195:4660-6.
- 451 [9] Tang Y, Liu J. Effect of anode and Boudouard reaction catalysts on the performance
452 of direct carbon solid oxide fuel cells. *International Journal of Hydrogen Energy*.
453 2010;35:11188-93.
- 454 [10] Cantero-Tubilla B, Xu C, Zondlo JW, Sabolsky K, Sabolsky EM. Investigation of anode
455 configurations and fuel mixtures on the performance of direct carbon fuel cells (DCFCs).
456 *Journal of Power Sources*. 2013;238:227-35.
- 457 [11] Xie Y, Cai W, Xiao J, Tang Y, Liu J, Liu M. Electrochemical gas-electricity cogeneration
458 through direct carbon solid oxide fuel cells. *Journal of Power Sources*. 2015;277:1-8.
- 459 [12] Xu H, Chen B, Zhang H, Sun Q, Yang G, Ni M. Modeling of direct carbon solid oxide
460 fuel cells with H₂O and CO₂ as gasification agents. *International Journal of Hydrogen*
461 *Energy*. 2017;42:15641-51.
- 462 [13] Alexander BR, Mitchell RE, Gür TM. Modeling of experimental results for carbon
463 utilization in a carbon fuel cell. *Journal of Power Sources*. 2013;228:132-40.
- 464 [14] Johnson DU, Mitchell RE, Gür TM. Modeling Power Production in a Tubular Carbon
465 Fuel Cell. *ECS Transactions*. 2014;61:235-43.
- 466 [15] Xu H, Chen B, Liu J, Ni M. Modeling of direct carbon solid oxide fuel cell for CO and
467 electricity cogeneration. *Applied Energy*. 2016;178:353-62.
- 468 [16] Xu H, Chen B, Zhang H, Sun Q, Yang G, Ni M. Modeling of direct carbon solid oxide
469 fuel cells with H₂O and CO₂ as gasification agents. *International Journal of Hydrogen*
470 *Energy*. 2017.
- 471 [17] Xu H, Chen B, Zhang H, Kong W, Liang B, Ni M. The thermal effect in direct carbon

solid oxide fuel cells. *Applied Thermal Engineering*. 2017;118:652-62.

[18] Xu H, Chen B, Tan P, Zhang H, Yuan J, Liu J, et al. Performance improvement of a direct carbon solid oxide fuel cell system by combining with a Stirling cycle. *Energy*. 2017;140:979-87.

[19] Chen L, Zhu X, Sun F, Wu C. Exergy-based ecological optimization of linear phenomenological heat-transfer law irreversible Carnot-engines. *Applied Energy*. 2006;83:573-82.

[20] Hosseinpour J, Sadeghi M, Chitsaz A, Ranjbar F, Rosen MA. Exergy assessment and optimization of a cogeneration system based on a solid oxide fuel cell integrated with a Stirling engine. *Energy Conversion and Management*. 2017;143:448-58.

[21] Garcia RF, Carril JC, Gomez JR, Gomez MR. Energy and entropy analysis of closed adiabatic expansion based trilateral cycles. *Energy Conversion and Management*. 2016;119:49-59.

[22] Luu MT, Milani D, McNaughton R, Abbas A. Analysis for flexible operation of supercritical CO₂ Brayton cycle integrated with solar thermal systems. *Energy*. 2017;124:752-71.

[23] Grelet V, Reiche T, Lemort V, Nadri M, Dufour P. Transient performance evaluation of waste heat recovery rankine cycle based system for heavy duty trucks. *Applied Energy*. 2016;165:878-92.

[24] Açıkkalp E. Performance analysis of irreversible molten carbonate fuel cell – Braysson heat engine with ecological objective approach. *Energy Conversion and Management*. 2017;132:432-7.

[25] Modi A, Kærn MR, Andreasen JG, Haglind F. Thermoeconomic optimization of a Kalina cycle for a central receiver concentrating solar power plant. *Energy Conversion and Management*. 2016;115:276-87.

[26] Lin J-C, Hou S-S. Effects of heat loss as percentage of fuel's energy, friction and variable specific heats of working fluid on performance of air standard Otto cycle. *Energy Conversion and Management*. 2008;49:1218-27.

[27] Curto-Risso PL, Medina A, Hernández AC. Theoretical and simulated models for an irreversible Otto cycle. *Journal of Applied Physics*. 2008;104:094911.

[28] Xia S, Chen L, Sun F. Maximum cycle work output optimization for generalized radiative law Otto cycle engines. *The European Physical Journal Plus*. 2016;131:394.

[29] Ge Y, Chen L, Sun F. Finite-time thermodynamic modelling and analysis of an irreversible Otto-cycle. *Applied Energy*. 2008;85:618-24.

[30] Gumus M, Atmaca M, Yilmaz T. Efficiency of an Otto engine under alternative power optimizations. *International Journal of Energy Research*. 2009;33:745-52.

[31] Chen J, Zhao Y, He J. Optimization criteria for the important parameters of an irreversible Otto heat-engine. *Applied Energy*. 2006;83:228-38.

[32] Zhao Y, Lin B, Chen J. Optimum Criteria on the Important Parameters of an Irreversible Otto Heat Engine With the Temperature-Dependent Heat Capacities of the Working Fluid. *Journal of Energy Resources Technology*. 2007;129:348-54.

[33] Chen L, Wu C, Sun F, Cao S. Heat transfer effects on the net work output and

efficiency characteristics for an air-standard Otto cycle. *Energy Conversion and Management*. 1998;39:643-8.

[34] Ge Y, Chen L, Sun F, Wu C. Thermodynamic simulation of performance of an Otto cycle with heat transfer and variable specific heats of working fluid. *International Journal of Thermal Sciences*. 2005;44:506-11.

[35] Ge Y, Chen L, Sun F, Wu C. The effects of variable specific heats of working fluid on the performance of an irreversible Otto cycle. *International Journal of Exergy*. 2005;2:274-83.

[36] Eldighidy SM. Optimum outlet temperature of solar collector for maximum work output for an Otto air-standard cycle with ideal regeneration. *Solar Energy*. 1993;51:175-82.

[37] Stempien JP, Liu Q, Ni M, Sun Q, Chan SH. Physical principles for the calculation of equilibrium potential for co-electrolysis of steam and carbon dioxide in a Solid Oxide Electrolyzer Cell (SOEC). *Electrochimica Acta*. 2014;147:490-7.

[38] Xu H, Chen B, Irvine J, Ni M. Modeling of CH₄-assisted SOEC for H₂O/CO₂ co-electrolysis. *International Journal of Hydrogen Energy*. 2016;41:21839-49.

[39] Ni M. 2D heat and mass transfer modeling of methane steam reforming for hydrogen production in a compact reformer. *Energy Conversion and Management*. 2013;65:155-63.

[40] Angulo-Brown F, Rocha-Martínez JA, Navarrete-González TD. A non-endoreversible Otto cycle model: improving power output and efficiency. *Journal of Physics D: Applied Physics*. 1996;29:80.

[41] Angulo-Brown F, Fernández-Betanzos J, Diaz-Pico CA. Compression ratio of an optimized air standard Otto-cycle model. *European Journal of Physics*. 1994;15:38.

[42] Aragón-González G, Canales-Palma A, León-Galicia A. Maximum irreversible work and efficiency in power cycles. *Journal of Physics D: Applied Physics*. 2000;33:1403.

[43] Sadrameli SM. Mathematical models for the simulation of thermal regenerators: A state-of-the-art review. *Renewable and Sustainable Energy Reviews*. 2016;58:462-76.

[44] Eguchi K, Setoguchi T, Inoue T, Arai H. Electrical-Properties of Ceria-Based Oxides and Their Application to Solid Oxide Fuel-Cells. *Solid State Ionics*. 1992;52:165-72.

[45] Luo Y, Shi Y, Li W, Cai N. Comprehensive modeling of tubular solid oxide electrolysis cell for co-electrolysis of steam and carbon dioxide. *Energy*. 2014;70:420-34.

[46] Yaqi L, Yaling H, Weiwei W. Optimization of solar-powered Stirling heat engine with finite-time thermodynamics. *Renewable Energy*. 2011;36:421-7.

[47] Ahmadi MH, Sayyaadi H, Dehghani S, Hosseinzade H. Designing a solar powered Stirling heat engine based on multiple criteria: Maximized thermal efficiency and power. *Energy Conversion and Management*. 2013;75:282-91.

552 **List of Tables**

553 Table 1. Model parameters used in DC-SOFC.

554 Table 2. Parameters used in Otto heat engine.

555 Table 3. Optimum value of compression ratio r_{opt} under different power dissipation b , the

556 other parameters are as the same in Table 1 and Table 2.

557

558 Table 1. Model parameters used in DC-SOFC [15, 44, 45].

Parameters	Value or expression	Unit
Ionic conductivity		
σ_{GDC}	$\frac{100}{T} \times 10^{(6.66071 - \frac{5322.92}{T})}$	S m^{-1}
σ_{YSZ}	$3.34 \times 10^4 e^{\frac{-10300}{T}}$	S m^{-1}
Electronic conductivity		
σ_{silver}	$\frac{1.59 \times 10^8}{(0.0038T - 0.1134)}$	S m^{-1}
Porosity		
ε_{an}	0.46	
ε_{ca}	0.46	
Electrode volume fraction		
V_{GDC}	0.21	
V_{silver}	0.79	
TPB length of electrode		
Anode	2.14×10^5	$\text{m}^2 \text{m}^{-3}$
Cathode	2.14×10^5	$\text{m}^2 \text{m}^{-3}$
Tortuosity		
τ_{an}	3	
τ_{ca}	3	
Exchange current density		
i_0^{CO}	450	A m^{-2}
$i_0^{\text{O}_2}$	400	A m^{-2}

Charge transfer coefficient		
α_{CO}	0.5	
α_{O_2}	0.5	
Equilibrium constant of Boudouard reaction	$k_{\text{rb}} = 6 \times 10^{13}$	1/s
Activation energy of Boudouard reaction	$E_{\text{rb}} = 248$	kJ mol ⁻¹

559

560

561 Table 2. Parameters used in Otto heat engine [46, 47].

Parameter	Value
Constant-volume heat capacity during the compression stroke, C_{V_1} (J K ⁻¹)	0.2988
Constant-volume heat capacity during the power stroke, C_{V_2} (J K ⁻¹)	0.4372
Constant temperature rate, K_1 (s K ⁻¹)	8.128×10^{-6}
Constant temperature rate, K_2 (s K ⁻¹)	1.867×10^{-5}
Compression ratio, r	9.26
Specific heat ratio, γ	1.4
Dissipation power due to friction b (W)	32.5

562

563

564 Table 3. Optimum value of compression ratio r_{opt} under different power dissipation b , the

565 other parameters are as the same in Table 1 and Table 2.

b (W)	0	16.25	32.5	48.75
r_{opt}	-	12.48	9.26	7.80

566

List of Figures

Fig. 1. Schematic diagram of (a) a DC-SOFC based system, (b) the heat and mass transfer process at small operating current density, and (c) the heat and mass transfer process at large operating current density.

Fig. 2. The curves of Q and V versus current density under different operating temperature, where $i_{in} = I_{in}/A$, A is the polar plate area of the DC-SOFC, V_{in} is the voltage corresponding to i_{in} .

Fig. 3. The pressure-volume diagram of the internal irreversible Otto cycle.

Fig. 4. The (a) efficiency, and (b) equivalent power density of the Otto heat engine under different operating conditions, where $P_{Otto}^* = P_{Otto}/A$ is the equivalent power density of the Otto heat engine.

Fig. 5. Equivalent power densities of the DC-SOFC, Otto heat engine and proposed system at (a) 1073 K, (b) 1123 K and (c) 1173 K.

Fig. 6. Equivalent efficiencies of the DC-SOFC, Otto heat engine and proposed system at (a) 1073 K, (b) 1123 K and (c) 1173 K.

Fig. 7. Effects of distance between carbon layer and anode electrode on the performance of the proposed system at 1123K.

Fig. 8. Effects of compression ratio on the performance of the proposed system at 1123 K.

Fig. 9. Effects of compression ratio and power dissipation of the Otto heat engine on the performance of the proposed system at 1123 K.

588 Fig. 1.

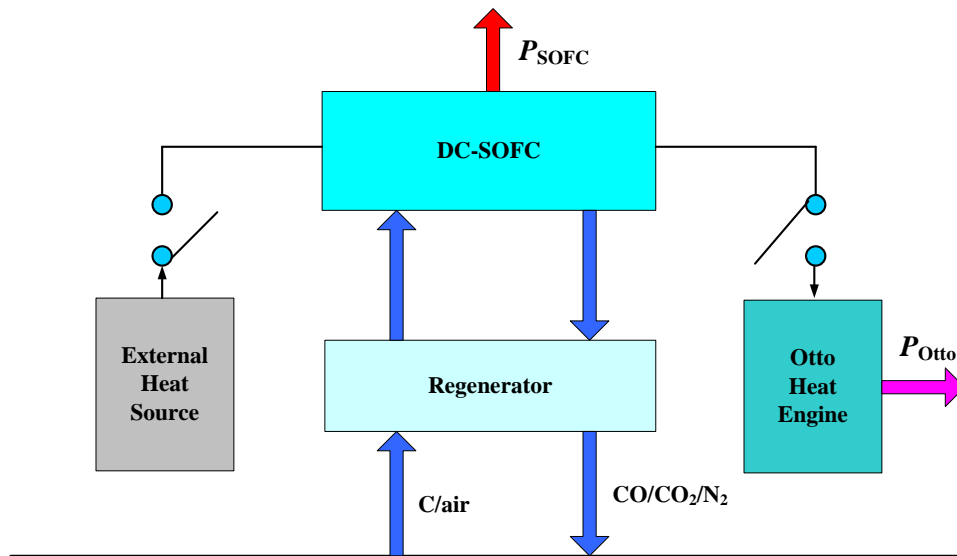


Fig. 1. (a) Schematic diagram of a DC-SOFC based system.

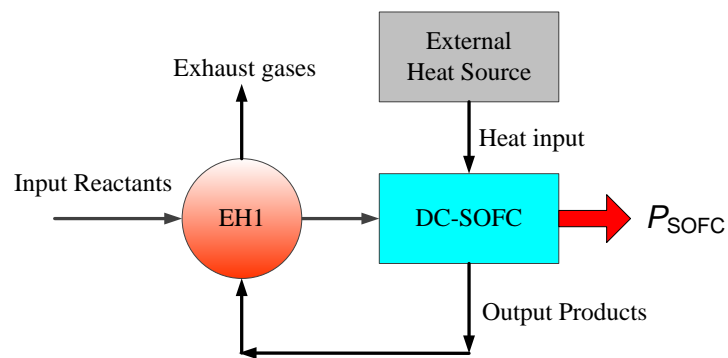
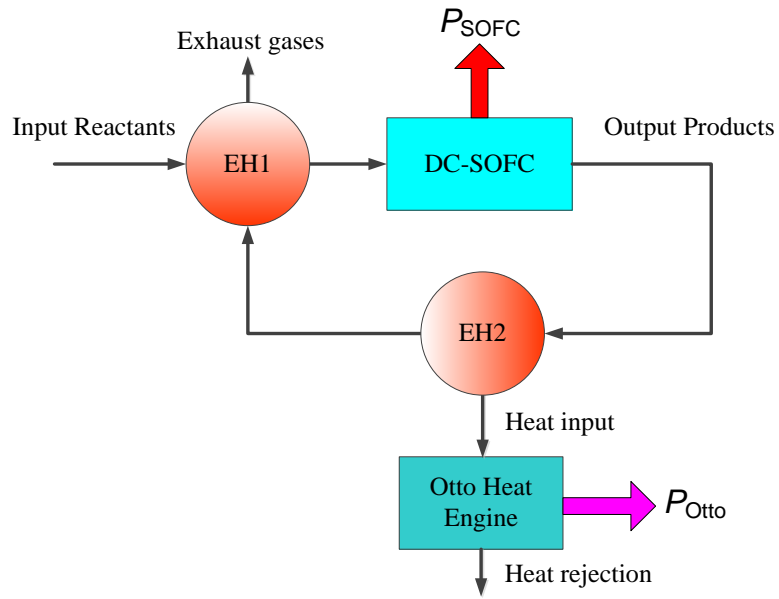


Fig. 1. (b) Schematic diagram of the heat and mass transfer process at small operating current density.



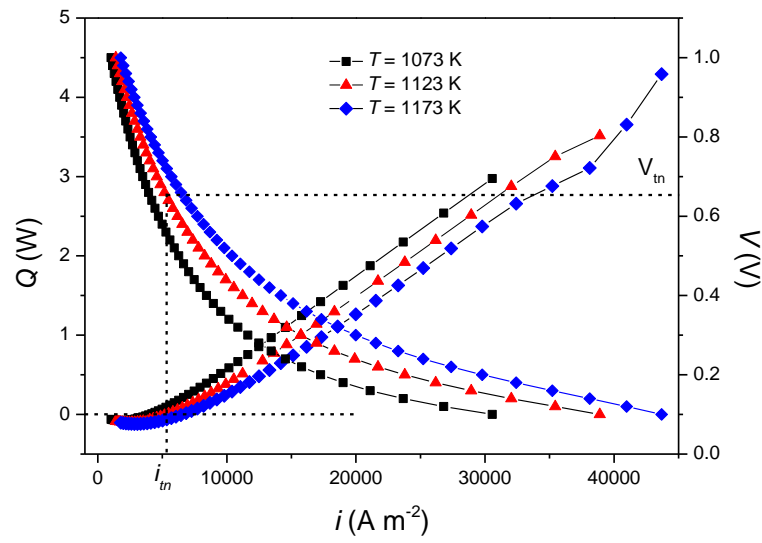
595

596 Fig. 1. (c) Schematic diagram of the heat and mass transfer process at large operating current

597 density.

598

599 Fig. 2.



600

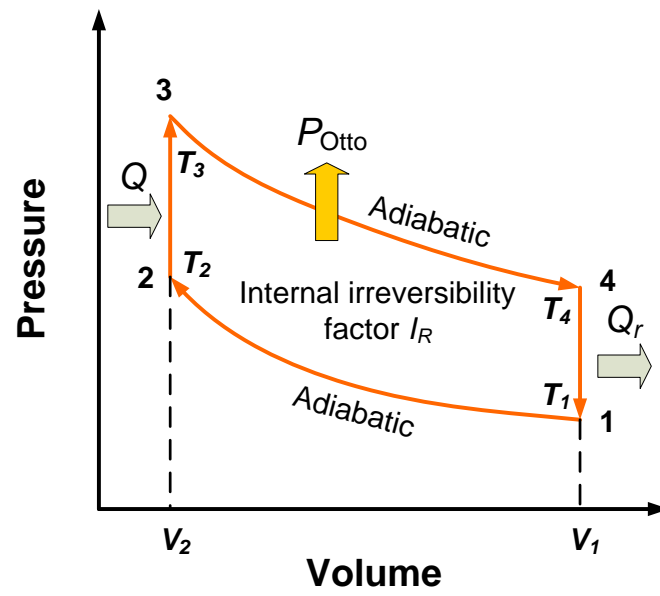
601 Fig. 2. The curves of Q and V versus current density under different operating temperature,

602 where $i_{tn} = I_{tn}/A$, A is the polar plate area of the DC-SOFC, V_{tn} is the voltage

603 corresponding to i_{tn} .

604

605 Fig. 3.



606

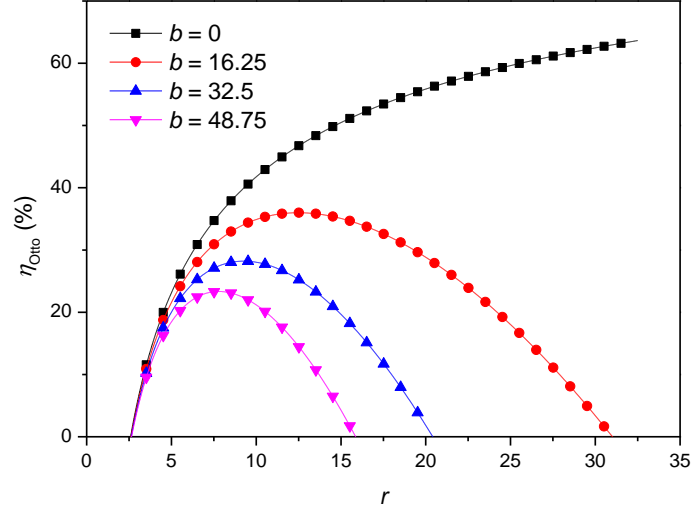
607 Fig. 3. The pressure-volume diagram of the internal irreversible Otto cycle.

608

609

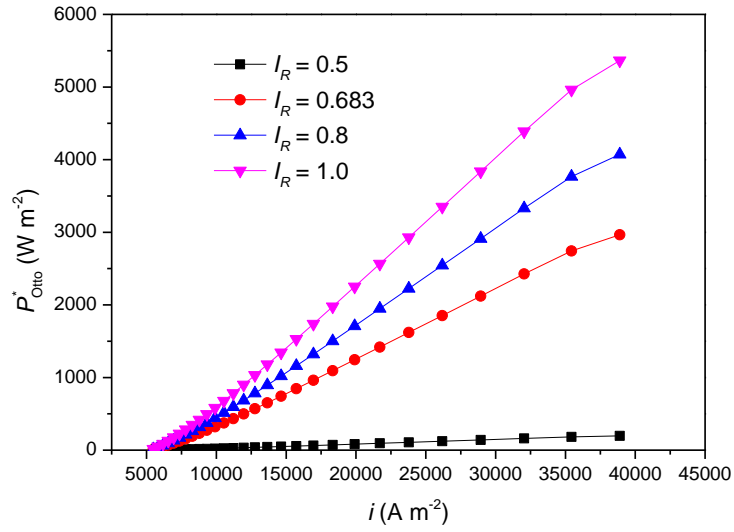
610 Fig. 4.

(a)



611

(b)



612

613 Fig. 4. The (a) efficiency, and (b) equivalent power density of the Otto heat engine under

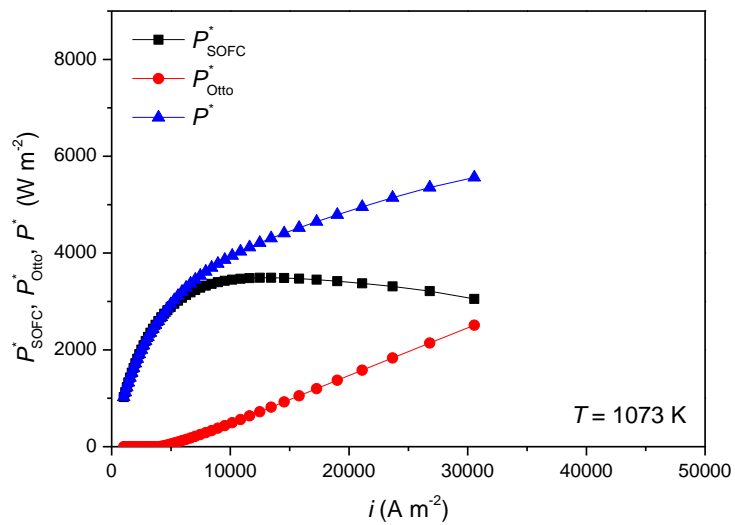
614 different operating conditions, where $P_{\text{Otto}}^* = P_{\text{Otto}} / A$ is the equivalent power density of the

615 Otto heat engine.

616

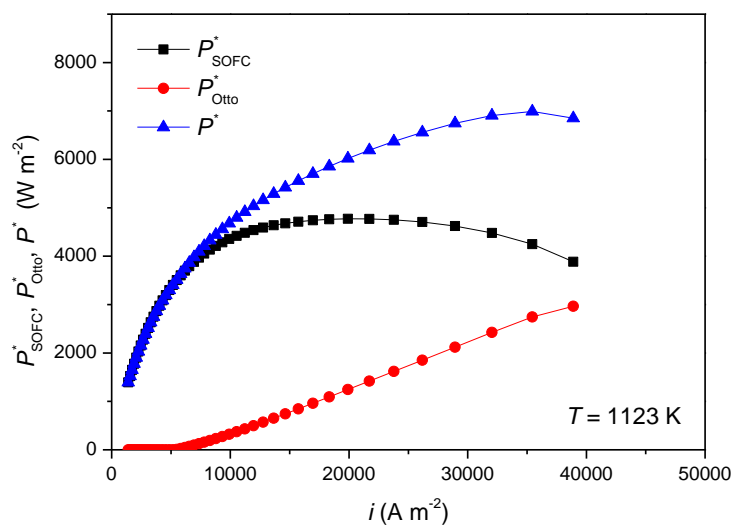
617 Fig. 5.

(a)



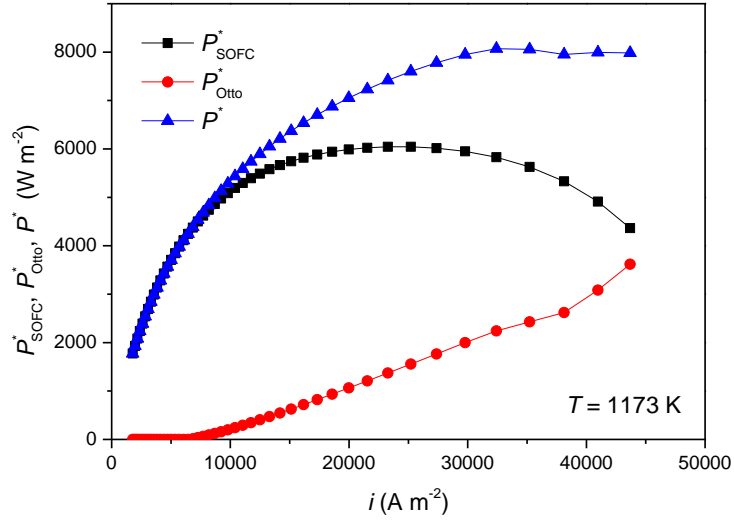
618

(b)



619

(c)



620

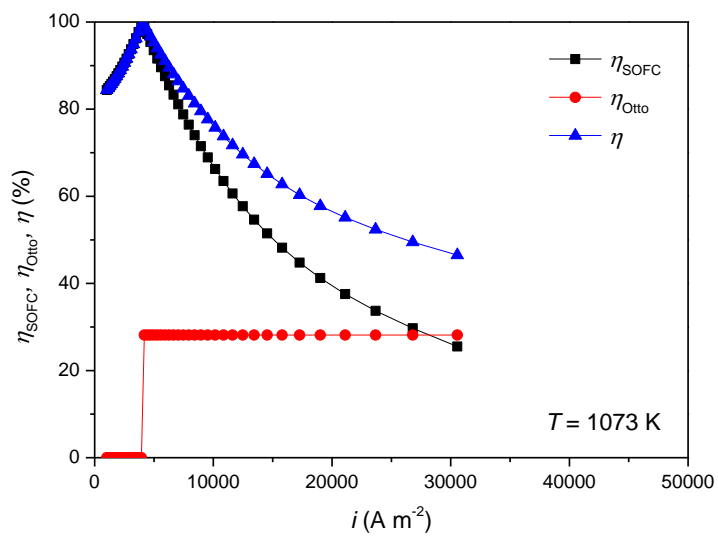
621 Fig. 5. Equivalent power densities of the DC-SOFC, Otto heat engine and proposed system at

622 (a) 1073 K, (b) 1123 K and (c) 1173 K.

623

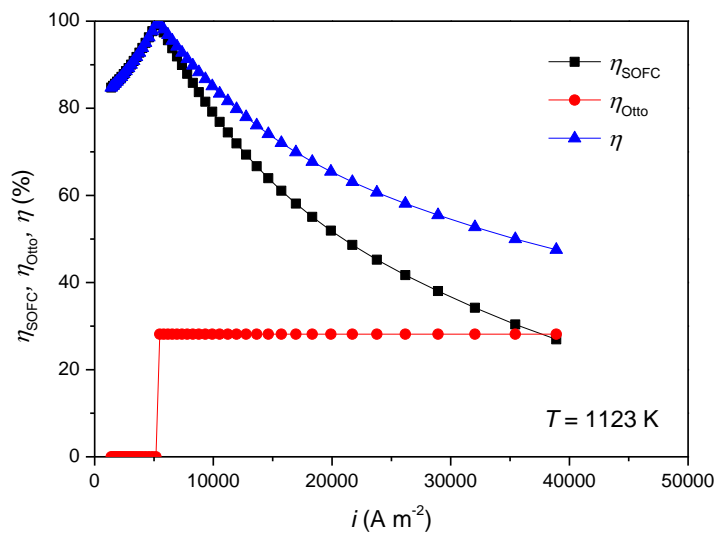
624 Fig. 6.

(a)



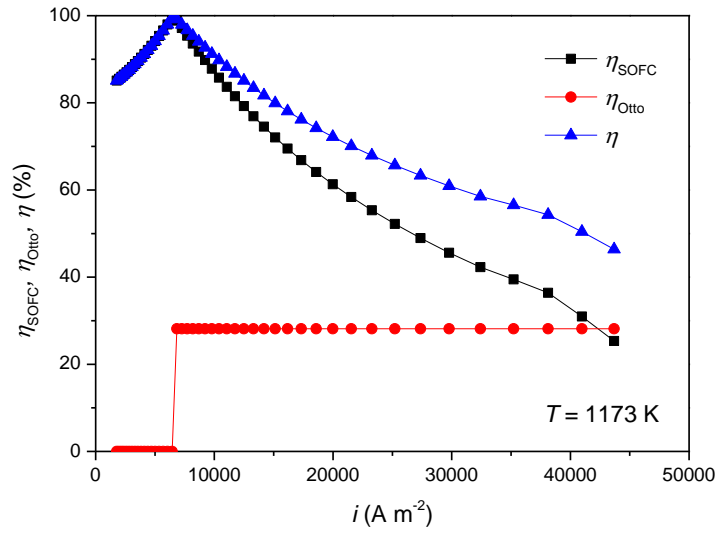
625

(b)



626

(c)



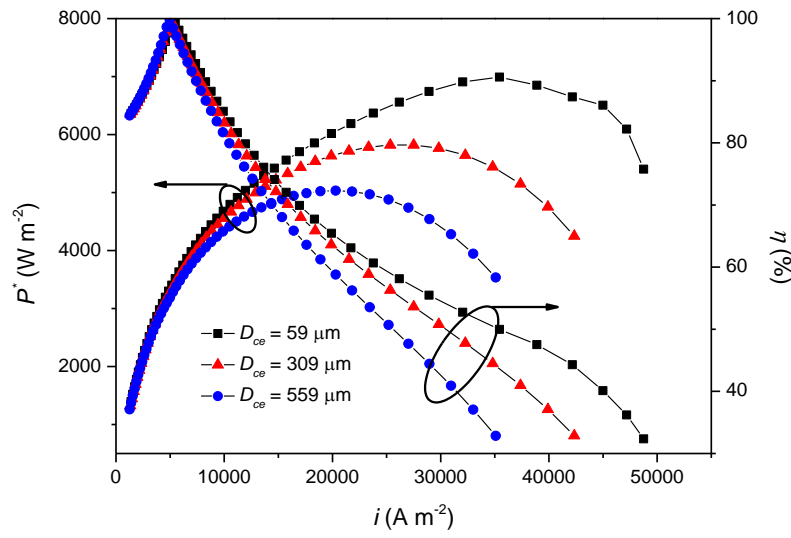
627

628 Fig. 6. Equivalent efficiencies of the DC-SOFC, Otto heat engine and proposed system at (a)

629 1073 K, (b) 1123 K and (c) 1173 K.

630

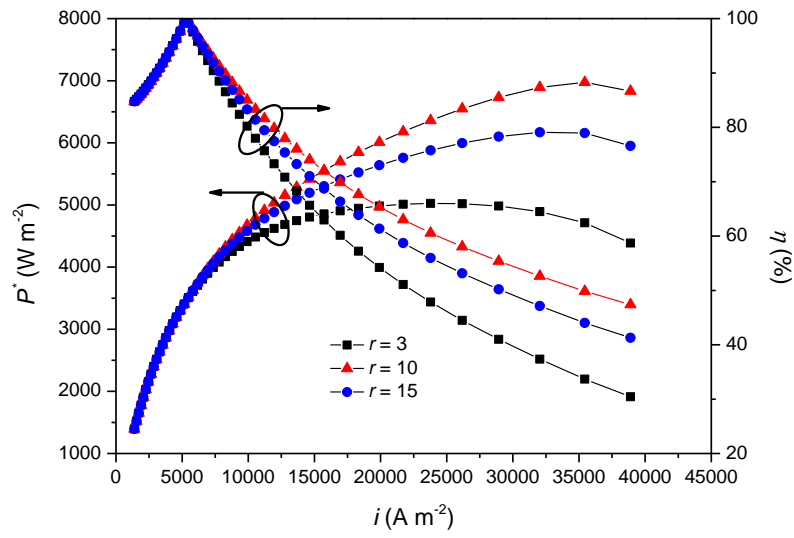
631 Fig. 7.



632
 633 Fig. 7. Effects of distance between carbon layer and anode electrode on the performance of the
 634 proposed system at 1123 K.

635

636 Fig. 8.

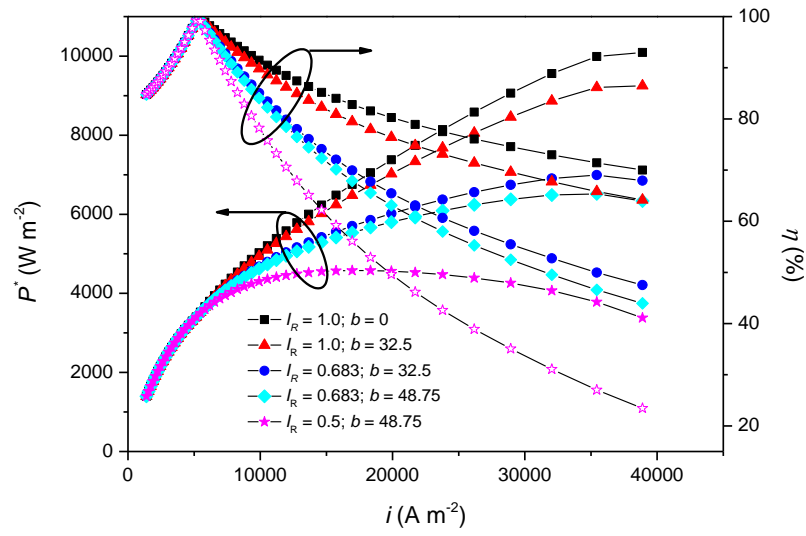


637

638 Fig. 8. Effects of compression ratio on the performance of the proposed system at 1123 K.

639

640 Fig. 9.



641
642 Fig. 9. Effects of compression ratio and power dissipation of the Otto heat engine on the
643 performance of the proposed system at 1123 K.

644